Contents lists available at ScienceDirect

Informatics in Medicine Unlocked

journal homepage: http://www.elsevier.com/locate/imu

Three-Dimensional OCT Compressed Sensing using the shearlet transform under continuous trajectories sampling

Bassel Haydar [a,c,*], Stéphane Chrétien [b,d], Adrien Bartoli [c], Brahim Tamadazte [a,e]

[a] FEMTO-ST Institute, University of Bourgogne Franche-Comté, CNRS, F-25000, Besangon, France
[b] ERIC Laboratory, University of Lyon, 2 5 avenue Mendes France 69676 Bron Cedex Office: 073, Bat: K, France
[c] PASCAL Institute, University of Clermont Auvergne, CNRS, F-63000, Clermont-Ferrand, France
[d] National Physical Laboratory, Data Science Division Hampton Road, Teddington, TW11 0LW, United Kingdom
[e] Institute for Intelligent Systems and Robotics, University of Sorbonne, CNRS, UMR 7222, 4 place Jussieu, 75005, Paris, France

ARTICLE INFO

Keywords:
Optical Coherence Tomography
Medical imaging
Compressed Sensing
Sparsity
Shearlet transform
Continuous scanning trajectories

ABSTRACT

Background: Optical Coherence Tomography (OCT) is an emerging medical imaging technology. It is well suited to various medical applications requiring tissue imaging with micrometer resolution and millimeter penetration depth such as in ophthalmology and dermatology. Despite its numerous advantages, OCT has a long acquisition time for high-resolution images or volumes. This paper deals with the development of a *Compressed, Sensing* (CS) paradigm for faster 3-dimensional OCT image acquisition.

Methods: The proposed framework includes three main steps: 1) defining a random-like and parameterizable and continuous scanning trajectories that must be compatible with a smooth mechanical scan, 2) rasterizing the scanning trajectory to make it achievable by a physical system (i.e. galvanometer mirrors), and 3) incorporating a high sparsifying data technique so-called 3D shearlet transform into the compressed sensing scheme. Actually, shearlet transform is mathematically optimal for multidimensional data decomposition and has been proven more efficient than classical ones such as those obtained by wavelet or curvelet transforms. Actually, shearlet system provides a very efficient tool for encoding anisotropic features (such as edges in images) in multivariate problem classes.

Results: Numerical simulations and *ex vivo* experiments were carried out. The obtained results showed the ability of the proposed method to recover OCT images and volumes with high fidelity for different subsampling rates and scanning schemes, demonstrating the relevance of the proposed approach.

1. Introduction

1.1. Overview and motivations

Optical Coherence Tomography is a powerful biomedical imaging technology that uses low coherent light to capture micrometer-scale resolution data from within optical scattering media (e.g., biological tissue). Actually, OCT data, sometimes called *optical biopsy,* can image a tissue at or near the resolution of the well-known histopathology procedure without the need for excisional biopsy. Consequently, the physician can take unlimited biopsies and reduce the need for *physical biopsy* that are more invasive and imply a delay in the interpretation, namely based on histopatho-logical examination. An OCT imaging device allows acquiring cross-sections in a non-destructive and contactless manner. Its operating principle is based on the use of low-coherence interferometry employing near infrared light Fujimoto, Pitris, Boppart and Brezinski [1]. Initially, the OCT technology was developed for the ophthalmology and optometry fields where it can be used to obtain detailed images from within the retina, because of the translucent nature, the minimal scattering, the good light-tissue interaction, and the high-light penetration characteristics of the retina. Recently, it has also begun to be used in interventional cardiology to help diagnose coronary artery disease as well as in dermatology Zysk, Nguyen, Oldenburg, Marks and Boppart [2].

There are two main families of **OCT** imaging techniques: Fourier-Domain **(FD) OCT** and Time-Domain **(TD)- OCT**. The **FD-OCT** method

* Corresponding author. FEMTO-ST Institute, University of Bourgogne Franche-Comté, CNRS, F-25000, Besangon, France.
E-mail addresses: bassel.haydar@femto-st.fr (B. Haydar), stephane.chretien@univ-lyon2.fr (S. Chrétien), adrien.bartoli@gmail.com (A. Bartoli), brahim.tamadazte@femto-st.fr (B. Tamadazte).

https://doi.org/10.1016/j.imu.2019.100287
Received 7 October 2019; Received in revised form 23 December 2019; Accepted 27 December 2019

is associated with high-speed scanning mechanism and better resolution as compared to the **TD-OCT**. In fact, the scan speed of **TD-OCT** systems depends on the mechanical cycle time of the moving reference mirror driver, whereas in **FD-OCT,** the reference mirror is fixed, which assists in sampling multiple points from the tissue structures, simultaneously Wang, Xia, Tian and Zhou [3]. As results**, FD-OCT** can provide higher resolution, and frame-rate compared to the **TD-OCT** Chen, Cense, Pierce, Nassif, Park, Yun, White, Bouma, Tearney and de Boer [4]. However, despite the superiority of **FD-OCT** systems over **TD-OCT** ones, it nevertheless has limitations for effective use in several medical applications. Effectively, **FD-OCT** offers a high frequency acquisition of **1D** (optical cores) and **2D** (cross-sections), however the required time for 3D data (OCT volume), their processing, transfer, and storage remains highly problematic. For instance, acquiring a volume of $10 \times 10 \times 3.5$ mm^3 using a standard **FD-OCT** system such as the Telesto II from Thorlabs®requires more than 1 min and 10Go of RAM (Random Access Memory) for preview limiting real-time diagnosis or tissue monitoring. Additionally, in **FD-OCT,** to discretize and digitize the spectral interferograms at high-resolution and frame-rate, it is necessary to use high-performance array detectors such as **CCD** (Charge-Coupled Device) sensors Choma, Sarunic, Yang and Izatt [5]. The use of these kind of sensors increases significantly the cost of an **FD-OCT** system and then limits their deployment in hospitals, particularly in developing countries.

To overcome certain limitations of using **OCT** imaging modality, namely when the use of **C-**scan acquisition is required, we explore the potential of developing of Compressed Sensing **(CS)** scheme in aim to:

- increase the frame-rate of OCT volume acquisition, namely for applications in assisted surgical guidance and intervention
- reduce the amount of data required and subsequent processing for high-resolution image reconstruction Liu and Kang [6];
- make possible to use smaller and less expensive array detectors, while guaranteeing spatial and axial resolutions that are faithful to those obtained by the expensive sensors usually used;
- reduce artifacts in OCT volumes mainly due to the low acquisition frame-time and possible physiological movements of the patient when it comes to *in vivo* examination.

Compressed Sensing was developed simultaneously by Donoho and Candès, Romberg and Tao Donoho [7]; Candès et al[36] who introduced randomized acquisition schemes and provided the strong mathematical underpinnings of CS theory. It consists of a paradigm which illustrates the possibility to acquire at sub-Nyquist rate and compress signals (measurements) all at the same time under sparsity assumptions, at the expense of potentially more involved computations for the recovery Foucart and Rauhut [9]. Sparsity, which is the opposite of density, is an essential feature shared by many wavelet-type decompositions, that is leveraged in CS theory Davenport and Duarte [10]. Most medical imaging systems, such as magnetic resonance imaging **(MRI)**, computed-tomography **(CT), OCT**, … are known to admit a high-level of sparsity in other decomposition bases such as wavelets, curvelets, shearlets, etc. This especially because that medical images are generally composed of large homogeneous areas with a low dynamic range in terms of contrast compared to conventional images Fei, Wei and Zongxi [11]. In addition, it is admitted to consider that the different medical imaging modalities (e.g., OCT) share the common feature of acquiring, totally or at least partially, the signals through spectral measurements of highly sparse signals. However, in many practical settings, natural sparsity is sometimes insufficient for accurate signal recovery and other tools have to be put to work in order to achieve better reconstruction in inverse problems of the CS type.

One of the necessary conditions for the feasibility of compressed acquisition is the ability to decompose efficiency the signal/image in a sparsifying functions bases such as wavelet, curvelet, shearlet transforms, etc. The latter have recently been introduced as a new decomposition that is superior, in many respects, to wavelet multiple scale decomposition Mallat [12]. Shearlet system Labate, Lim, Kutyniok and Weiss [13] provides an efficient compactly supported decomposition which extends the wavelet decomposition and was proved to outperform the wavelet decomposition in many applications such as sparsifying method. A notable feature of shearlet is that it can encode curvilinear singularities and others anisotropic features in a much better fashion than wavelet functions can do. As a result, shearlet provides a more precise separation of the morphologically distinct features of points and curves. Whereas wavelet systems are obtained using dyadic scaling and translations of a single function shearlet systems can be generated using a single operator including parabolic scaling, shearing, and translation operators Kutyniok and Labate [14]. From the point-of-view of CS, shearlet systems provide a high-sparsity representation of the signal, which is practically often optimal, a considerable advantage over other techniques such as Fourier and wavelet transforms.

1.2. Contributions

Most of the existing CS methods requires the use of incoherent pseudo-random or random subsampling of k-sparse data Candes, Romberg and Tao [8]; Candes [15]. These subsampling schemes (also called masks or sensing matrices) are often of little relevance since they cannot be implemented on physical acquisition systems Bigot, Boyer and Weiss [16]. In OCT context, the acquisition is processed through *xy* scanning scheme performed by a two degrees-of-freedom (dof) galvanometer mirror device and random sampling which leads to the fact that is inconsistent with the physical constraints that preclude the use of non-smooth trajectories. Consequently, in case of a physical implementation, acquiring few measurements in a random sampling method can result in a longer computation time in comparison to the acquisition of all data in raster mode.

In this paper, we investigate novel scanning schemes using continuous trajectories (e.g., spiral, rosette, and Lissajous), that consider the limitations imposed by the OCT mirrors in terms of scanning speed, scan area, and kinematics. We also develop a rasterization strategy which ensures that pixel coordinates are optimally chosen to follow the predefined trajectory (i.e., *xy* positions) on the sample to be scanned.

Our implementation bridges our new scanning schemes with the existing digital shearlet transform toolbox provided by Kutyniok, Lim and Reisenhofer [17]. Our scanning schemes are based on spiral, rosette or Lissajous shaped trajectories that offer rapid and efficient coverage of the *k*-space. The proposed rasterization algorithm is embedded into our package and is designed to permit handy tuning of the subsampling rate, the scan area, and the variable density sampling along the trajectory. Finally, the developed methodology is shown to outperform current state of the art in the two following scenarios: 1) using a simulation based numerical validation framework in both 2D cross-sectional OCT image and 3D OCT volumes cases, and 2) using an experimental set-up equipped with a Fourier-Domain OCT device.

The rest of this paper is organized as follows. In Section 2, we present the Compressed Sensing framework, the sparsity representation as well as the shearlet transform. Also, the acquisition schemes, the proposed subsampling continuous trajectories, and the rasterization algorithm, both the sparsity and the incoherence are detailed in this section. Section 3 deals with the numerical validation when Section 4 discusses the experimental validations of the proposed methods and materials. Finally, a discussion on the obtained results with regard to the state-of-the-art is also provided.

2. Materials and methods

2.1. Compressed Sensing

Compressed Sensing was discovered in the breakthrough papers by

E. Candes, J. Romberg, T. Tao and D. Donoho [7]; Candes et al. [36] that created via a mathematical *tour de force,* a new paradigm for joint signal acquisition and compression and explored its tight relationships with modern optimization and random matrix theory. It has subsequently triggered an extensive research effort exploiting sparse representation of signals and images via fast orthogonal and even non-orthogonal decomposition such as wavelet transforms. CS initially attracted the signal processing community's attention after Candes and Donoho were able to show how to use random sampling in order to break the Nyquist barrier that had set the what used to be thought of as the sampling frequency limit to any data acquisition procedure. Then, the theory developed into richly ramified research field Foucart and Rauhut [9] with a versatile set of mathematical and algorithmic tools for efficient sampling of inherently sparse objects.

In mathematical terms, the problem can be stated as follows. Let x be an object (a vector, a matrix or a tensor) in a Euclidean space $\mathbb{E}$ which admits a k-sparse representation in a dictionary Γ, i.e.,

$$x = \sum_{j=1}^{q} c_j \Gamma_j \tag{1}$$

where $c \in \mathbb{R}^q$ is a k-sparse vector, which means that a vector with no more than k nonzero components. The observations are simply given by linear measurements of the form

$$y_i = \langle m_i, x \rangle$$

where $\langle m_i, \cdot \rangle$ is a functional on the $\mathbb{E}$ for $i = 1, \ldots, n$, and we obtain a linear system

$$y = \boldsymbol{A}c \tag{2}$$

where $\boldsymbol{A} \in \mathbb{R}^{n \times q}$ and the rows of $\boldsymbol{A}$ are given by

$$\boldsymbol{A}_{i,} := m_i^t \Gamma; i = 1, \ldots, n$$

In a CS type of problem, our goal is to recover the sparse vector c of components with as few observations (i.e., measures) as possible and therefore n will be thought as small compared to q. The main challenge is then to construct an observation matrix $\boldsymbol{A}$, which allow recovering x with n as small as possible for given values of k and m.

The CS problem can be solved unambiguously if there is no sparser solution to the linear system (2) than c. Thereby, recovery is obtained by simply finding the sparsest solution to (2). If for any c in $\mathbb{R}^q$ we denote by $||c||_0$ the l_0-norm of c, i.e. the cardinal of the set of indices of nonzero components of c, the CS problem is equivalent to

$$\min_{c \in \mathbb{R}^q} \|c\|_0 \quad \text{s.t.} \quad \boldsymbol{A}c = y \tag{3}$$

Let us denote by $\Delta_0(y)$, the solution of problem (3) and $\Delta_0(y)$ is called a decoder.[1] Thus, the CS problem may be viewed as a combinatorial optimization problem. Moreover, the following lemma is well known.

Lemma 1. *(see for instance Cohen, Dahmen and DeVore [18] If $\boldsymbol{A}$ is any $n \times p$ matrix and $2k \leq n$, then the following properties are equivalent:*

- *The decoder Δ_0 satisfies $\Delta_0(\boldsymbol{A}c) = c$, for all $c \in \Sigma_k$,*
- *For any set of indices T with $\#T = 2k$, the matrix $\boldsymbol{A}_T$ has rank* 2k where $\mathbf{A}_\mathrm{T}$ stands for the submatrix of **A** composed of the columns indexed by T only.

[1] 'In the general case where c is not the unique sparsest solution of (3) using this approach for recovery is of course possibly not relevant. Moreover, in such a case, this problem has several solutions with equal l_0-"norm" and one may rather define $\Delta_0(y)$ as an arbitrary element of the solution set.

2.2. The l_1 relaxation is given by

$$\min_{c \in \mathbb{R}^p} \|c\|_1 \quad \text{s.t.} \quad \boldsymbol{A}c = y \tag{4}$$

In the following, we will denote by $\Delta_1(y)$ the solution of the l_1-relaxation (4). From the computational viewpoint, this relaxation is of great interest since it can be solved in polynomial time. Indeed, (4) is equivalent to the linear program

The main subsequent problem induced by this choice of relaxation is to obtain easy-to-verify sufficient conditions on $\boldsymbol{A}$ for the relaxation to be exact, i.e. to produce the sparsest solution to the underdetermined system (2). An algebraic condition was given by Candès, Romberg and Tao Candès et al. [36]; called Restricted Isometry Property (RIP). We say that a matrix A satisfies the $RIP_{k,\delta}$ if, for every index subset S with cardinality $|S| \leq k$, and every $c \in \mathbb{R}^q$

$$(1-\delta)\|c_S\|_2 \leq \|\boldsymbol{A}_S c_S\|_2 \leq (1+\delta)\|c_S\|_2 \tag{5}$$

The smallest value of δ in the previous inequalities is denoted by δ_k. Up to now, this condition could only be proved to hold with great probability in the case where $\boldsymbol{A}$ is a sub Gaussian random matrix. Several algorithmic approaches have also been recently proposed in order to guaranty exactness of the l_1 relaxation such as in Juditsky and Nemirovski [19] and d'Aspremont and El Ghaoui [20]. A different approach to the study of decoder Δ_1 is based on the notion of incoherence. The coherence $\mu(\boldsymbol{A})$ of the observation matrix A is the largest absolute value among all scalar products of different columns of $\boldsymbol{A}$, i.e.

$$\mu(\boldsymbol{A}) = \max_{j \neq j'} \frac{|\langle \boldsymbol{A}_j, \boldsymbol{A}_{j'} \rangle|}{\|\boldsymbol{A}_j\|_2 \|\boldsymbol{A}_{j'}\|_2} \tag{6}$$

The matrix $\boldsymbol{A}$ is said to be incoherent when its coherence $\mu(\boldsymbol{A})$ is on the order of $1/\log(q)$. Several results have been obtained that guarantee exact recovery under the low coherence assumption.

In the noisy setting, the observation is given by

$$y_i = \langle m_i, x \rangle + \varepsilon_i \tag{7}$$

and the problem can be addressed by solving

$$\min_{c \in \mathbb{R}^q} \frac{1}{2}\|y - \boldsymbol{A}c\|_2^2 + \lambda \|c\|_1 \tag{8}$$

for specific values of $\lambda \in \mathbb{R}_+$. Exact recovery cannot hold in this setting, but using incoherence, exact recovery of the support of c was proved in Candès, Plan et al. [21] in the case where the variance of the noise is known beforehand, and in Chrétien and Darses [22] in the case of unknown variance. The main result from Chrétien and Darses [22] is

Theorem 2.1. *Set $\alpha > 0$ and $q \geq e^{8/\alpha}$. Let X satisfy the Generic Condition from Chrétien and Darses* [22]. *Let Assumption 2.1, 2.2, 2.3 and 2.4 from Chrétien and Darses* [22] *hold with*

$$n \geq \alpha(C_\mathrm{o} \log q + 1). \tag{9}$$

Then the probability that the estimator $\widehat{\beta}$ defined by (8) *with λ satisfying*[2]

$$\lambda^2 = C_{\mathrm{var}} \frac{\|y - X\widehat{\beta}\|_2^2}{n} \log q \tag{10}$$

where a relevant range for C_{var} is given by

$$C_{\mathrm{var}} \in \left[\frac{(1-r)^2}{20(1+r)C_{\mathrm{spar}}} \frac{n}{q}\|X\|^2; \frac{(1-r)^2}{2(1+r)C_{\mathrm{spar}}} \frac{n}{q}\|X\|^2 \right] \tag{11}$$

exactly recovers the support and sign pattern of β is greater than $1\text{–}228/q^{\alpha}$.

[2] note that this eqnarray is implicit since β depends on λ, but on the other hand, good algorithms for tuning A exist as shown in Chretien and Darses [22].

Another approach for fast reconstruction makes use of the Iterative Hard Thresholding algorithm Blumensath and Davies [23]. This algorithm is defined by the iterations

$$c^{(l+1)} = T_k\left(c^{(l)} + \boldsymbol{A}^t\left(y - \boldsymbol{A}c^{(l)}\right)\right) \tag{12}$$

where T_k is the threshold operator which sets all components to zero except for the k largest among them. Furthermore, the main result from Blumensath and Davies [23] is the following theorem.

Theorem 2.2. *Let $c^{\#}$ denotes the best k-term approximation of c. By assuming that A satisfies the RIP property with $\delta_{3k} < 1/\sqrt{32}$, then, for all I, we have*

$$\left\|c^{(l+1)} - c\right\|_2 \le 2^{-l}\|c^{\#}\|_2 + \tilde{\varepsilon} \tag{13}$$

where

$$\tilde{\varepsilon} = \|c - c^{\#}\|_2 + \frac{1}{\sqrt{k}}\|c - c^{\#}\|_1 + \|\varepsilon\|_2 \tag{14}$$

The Iterative Hard Thresholding algorithm can also be studied from the point of view of incoherence. A breakthrough result of Maleki Maleki [24] is the following Theorem.

Theorem 2.3. *Suppose that k $k \le 1/(3.1\mu(A))$ and $|c_j/c_{j+1}| < 3^{l_i-4}3^{l_j}$, $i = 1, \ldots, k$. Then, the Iterative Hard Thresholding algoritm finds the support of c in at most $\sum_{i=1}^{k} l_i + k$ iterations.*

Finally, choosing between different estimators is always a matter of finding the good balance between several technological constraints. In the rest of this paper, we will use the Iterative Hard Thresholding method for estimating the sparse vector c. The reason for this choice is that Iterative Hard Thresholding is lighter and faster than solving the LASSO problem (8).

2.3. Sparse representations

Sparsity is essential to the CS approach to reconstruction with few samples. In order to ensure the sparsity condition, it is necessary to represent the image in a suitable basis such as wavelet, curvelet or shearlet systems. In this work, we opted for the use of the shearlet transform, denoted by Θ, for the sparse representation of the OCT images, because shearlet transform was observed to achieve the best sparsity among these three options. To demonstrate this, we applied successive decompositions of the "Lena" photography having the resolution of 512 × 512 pixels, using wavelet, curvelet, shearlet transforms, respectively. As can be highlighted in Fig. 1, the shearlet method outperforms both the wavelet and the curvelets ones as summarized in the following:

- wavelet transform: $\approx 15 \times 10^4$ null-coefficients;
- curvelet transform: $\approx 5 \times 10^5$ null-coefficients;
- shearlet transform: $\approx \mathbf{2 \times 10^6}$ **null-coefficients.**

In a recent work, we also demonstrated experimentally that shearlet decomposition outperforms both the wavelet and the curvelet Duflot, Krupa, Tamadazte and Andreff [25].

2.4. Shearlet system

Shearlet theory provides an efficient mathematical tool for sparse image representation including geometry and multiscale analysis. It is considered as an extension of the wavelet transform, achieved by increasing their directional sensitivity in order to be more adapted for anisotropic image objects (e.g., edges and key points). Indeed the shearlet coefficients can be obtained by applying three successive anisotropic operations: dilation $\boldsymbol{D}_{\mathbf{E}}$ and $\boldsymbol{D}_{\tilde{\mathbf{E}}}$, shearing $\boldsymbol{D}_{\mathbf{S}_s}$ and translation (shift) $\boldsymbol{G}_{\mathbf{g}}$ on a finite number of generating functions $\psi, \tilde{\psi} \in L^2(\mathbb{R}^2)$. The anisotropic operators are defined using the following matrices.

The anisotropic dilation and shearing matrices are defined by:

- dilation: $\mathbf{E} = \mathrm{diag}(2, \sqrt{2})$ and $\tilde{\mathbf{E}} = \mathrm{diag}(\sqrt{2}, 2)$
- shearing: $\mathbf{S}_s = \begin{pmatrix} 1 & s \\ 0 & 1 \end{pmatrix}, s \in \mathbb{Z}$
- translation: $G_g h(\mathbf{p}) = h(\mathbf{p} - \mathbf{g}), (\mathbf{p}, \mathbf{g}) \in (\mathbb{R}^2)^2$, where $\mathbf{g}$ is xy translation vector, h is a function defined in $L^2(\mathbb{R}^2)$, and $\mathbf{p}$ represents the image-point coordinates.

Note that, the operator $\mathbf{S_s}$ is used instead of the rotation parameter, namely used in a curvelet transform Candes and Donoho [26]; which can be considered as a significant advantage for discretization, as the integer lattice is invariant under the shear operator for any $s \in \mathbb{Z}$. In other words, similarly to wavelet support, it unified the treatment of the continuous and digital shearlet theory, which leads to a fast implementation of the shearlet system. These operators are used in the following definition of a discrete shearlet system Kittipoom, Kutyniok and Lim [27].

Note that for a 2-dimensional scaling function $\varphi \in L^2(\mathbb{R}^2)$, and generating shearlet $\psi, \tilde{\psi} \in L^2(\mathbb{R}^2)$, a so-called cone-adapted shearlet system can be defined in order to cover the whole frequency plane S. and G [28]. Therefore, it is important to choose the generating shearlet functions ψ and $\tilde{\psi}$ such that they are supported in different frequency cones as depicted in Fig. 2.

In the following, we will describe the mathematical background of the cone-adapted shearlet system that inspired our work. Note that in contrast to the standard discrete transform, it has a direction bias which allows separating the low-frequency region with a square centered around the origin Kutyniok and Labate [14] as can be seen in Fig. 2.

By considering the scaling function φ, the generating functions ψ, $\tilde{\psi}$and the sampling constants $\mathbf{b} = (b_1, b_2) \in \mathbb{R}^+ \times \mathbb{R}^+$, the shearlet system is defined as

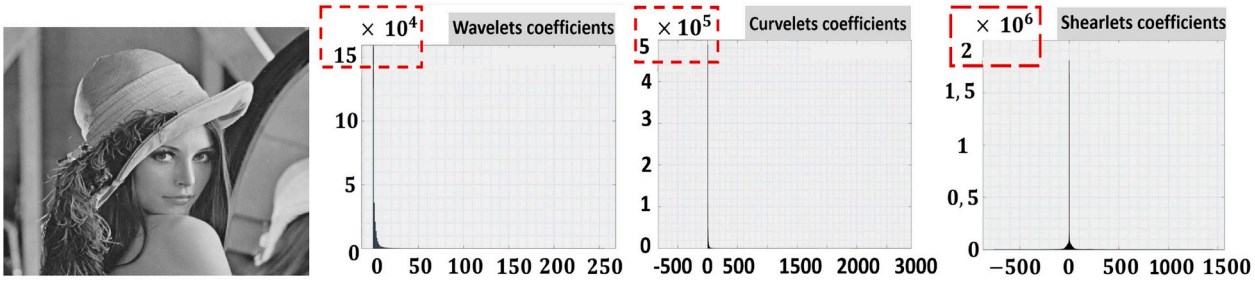

(a) Lena (b) wavelet coefficients (c) curvelet coefficients (d) shearlet coefficients

Fig. 1. *Sparsity comparison between wavelet, curvelet, and shearlet supports using Lena photography as benchmark. Note that, the histogram obtained by plotting the computed coefficients, sorted by their decreasing absolute values. One can reminder that the more the decomposition offer a large number of null-coefficients (or close to zero), the more the method allows a higher sparsity.*

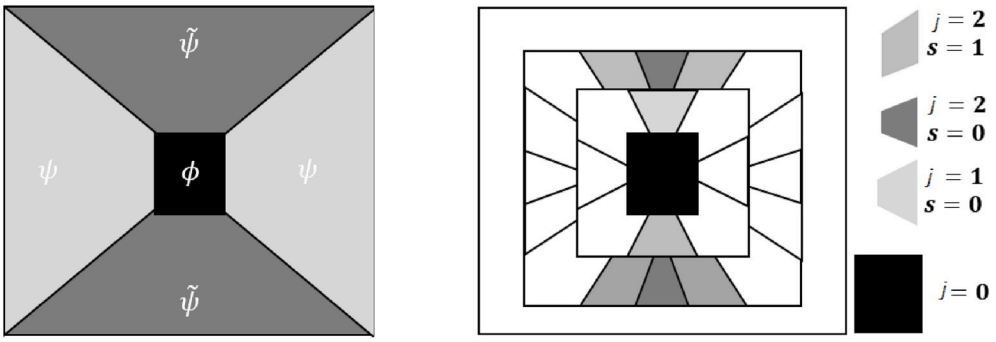

(a) decomposition of the frequency domain into cones (b) frequency tiling of the cone-adapted generated by shearlet system

Fig. 2. Illustration of the fundamental working of a cone-adapted continuous shearlet system. The latter is able efficiently cover whole $\mathbb{R}^2$ and giving equal treatment of all directions.

$$\boldsymbol{\Theta}(\varphi,\psi,\tilde{\psi},\mathbf{b}) = \Phi(\varphi,b_1)\cup\Psi(\psi,\mathbf{b})\cup\tilde{\Psi}(\tilde{\psi},\mathbf{b}) \tag{15}$$

where,

$$\Phi(\varphi,b_1) = \left\{G_{b_1\mathbf{g}}\varphi,\mathbf{g}\in\mathbb{Z}^2\right\} \tag{16}$$

$$\Psi(\psi,\mathbf{b}) = \left\{\psi_{j,s,\mathbf{g}} : j\geq 0, |s|\leq \left\lceil 2^{\frac{j}{2}}\right\rceil, \mathbf{g}\in\mathbb{Z}^2\right\} \tag{17}$$

$$\tilde{\Psi}(\tilde{\psi},\mathbf{b}) = \left\{\tilde{\psi}_{j,s,\mathbf{g}} : j\geq 0, |s|\leq \left\lceil 2^{\frac{j}{2}}\right\rceil, \mathbf{g}\in\mathbb{Z}^2\right\} \tag{18}$$

and

$$\psi_{j,s,\mathbf{g}} = D_{\mathrm{E}}^{j}D_{\mathbf{S}_s}G_{\mathbf{B}_\mathbf{g}}\psi \tag{19}$$

$$\tilde{\psi}_{j,s,\mathbf{g}} = D_{\mathrm{E}}^{j}D_{\mathbf{S}_s^t}G_{\tilde{\mathbf{B}}_\mathbf{g}}\tilde{\psi} \tag{20}$$

with $\mathbf{B}$ = diag(b_1,b_2), $\tilde{\mathbf{B}}$ = diag(b_2,b_1) and $\lceil\cdot\rceil$ denoting the ceiling function. Also, $|s|\leq\left\lceil 2^{\frac{j}{2}}\right\rceil$ is an important condition which allows varying the orientation of the shearlet support up to $\frac{\pi}{4}$.

It can be observed that the low frequency region is associated to $\Phi(\varphi, b_1)$, when both the horizontal and the vertical cones correspond to $\Psi(\psi,\mathbf{b})$ with $\tilde{\Psi}(\tilde{\psi},\mathbf{b})$ (Fig. 2).

Furthermore, the straightforward generalization of 2D shearlet is the 3D decomposition framework defined below. First, let us consider the 3-dimensional scaling function $\varphi\in L^2(\mathbb{R}^3)$, generating shearlet $\psi,\tilde{\psi},\widehat{\psi}\in L^2(\mathbb{R}^3)$, and the sampling constants $\mathbf{b} = (b_1,b_2,b_2)\in\mathbb{R}^+\times\mathbb{R}^+\times\mathbb{R}^+$ for which a so-called *pyramid-adapted* discrete shearlet system is defined as

$$\boldsymbol{\Theta}(\varphi,\psi,\tilde{\psi},\widehat{\psi},\mathbf{b}) = \Phi(\varphi,b_1)\cup\Psi(\psi,\mathbf{b})\cup\tilde{\Psi}(\tilde{\psi},\mathbf{b})\cup\widehat{\Psi}(\widehat{\psi},\mathbf{b})$$

where the sets

$$\Phi(\varphi,b_1) = \left\{G_{b_1\mathbf{g}}\varphi,\mathbf{g}\in\mathbb{Z}^3\right\} \tag{21}$$

$$\Psi(\psi,\mathbf{b}) = \left\{\psi_{j,s,\mathbf{g}} : j\geq 0, |s_1|,|s_2|\leq 2^{\frac{j}{2}}, \mathbf{g}\in\mathbb{Z}^3\right\} \tag{22}$$

$$\tilde{\Psi}(\tilde{\psi},\mathbf{b}) = \left\{\tilde{\psi}_{j,s,\mathbf{g}} : j\geq 0, |s_1|,|s_2|\leq 2^{\frac{j}{2}}, \mathbf{g}\in\mathbb{Z}^3\right\} \tag{23}$$

$$\widehat{\Psi}(\widehat{\psi},\mathbf{b}) = \left\{\widehat{\psi}_{j,s,\mathbf{g}} : j\geq 0, |s_1|,|s_2|\leq 2^{\frac{j}{2}}, \mathbf{g}\in\mathbb{Z}^3\right\} \tag{24}$$

and

$$\boldsymbol{\psi}_{j,s,\mathbf{g}} = \boldsymbol{D}_{\mathrm{E}}^{j}\boldsymbol{D}_{\mathbf{S}_s}G_{\mathbf{B}_\mathbf{g}}\boldsymbol{\psi} \qquad \tilde{\boldsymbol{\psi}}_{j,s,\mathbf{g}} = \boldsymbol{D}_{\mathrm{E}}^{j}\boldsymbol{D}_{\tilde{\mathbf{S}}_s}\boldsymbol{G}_{\tilde{\mathbf{B}}_\mathbf{g}}\tilde{\boldsymbol{\psi}} \qquad \widehat{\boldsymbol{\psi}}_{j,s,\mathbf{g}} = \boldsymbol{D}_{\widehat{\mathrm{E}}}^{j}\boldsymbol{D}_{\widehat{\mathbf{S}}_s}\boldsymbol{G}_{\widehat{\mathbf{B}}_\mathbf{g}}\widehat{\boldsymbol{\psi}} \tag{25}$$

with $\mathbf{B}$ = diag(b_1, b_2, b_2), $\tilde{\mathbf{B}}$ = diag(b_2, b_1, b_2), so the scaling matrices are obtained as follows

$$\mathbf{E} = \mathrm{diag}\left(2,\sqrt{2},\sqrt{2}\right),\quad \tilde{\mathbf{E}} = \mathrm{diag}\left(\sqrt{2},2,\sqrt{2}\right),\quad \widehat{\mathbf{E}} = \mathrm{diag}\left(\sqrt{2},\sqrt{2},2\right), \tag{26}$$

and shearing matrices

$$\mathbf{S}_s = \begin{pmatrix}1 & s_1 & s_2\\ 0 & 1 & 0\\ 0 & 0 & 1\end{pmatrix},\quad \tilde{\mathbf{S}}_s = \begin{pmatrix}1 & 0 & 0\\ s_1 & 1 & s_2\\ 0 & 0 & 1\end{pmatrix},\quad \widehat{\mathbf{S}}_s = \begin{pmatrix}1 & 0 & 0\\ 0 & 1 & 0\\ s_1 & s_2 & 1\end{pmatrix}, s_1,s_2\in\mathbb{Z} \tag{27}$$

As results, the shearlet transform allows decomposing an OCT image (respectively, a volume) in a sparse basis as coefficients.

2.5. Scanning trajectories

As mentioned in the introduction, usually, the literature related to the compressed sensing methods in imaging, almost all have one characteristic in common: the use of pseudo-random or random subsampling scheme to select the k-sparse data that will reconstructed Rauhut [29]; Candes and Plan [30]. This methodology is suitable for image sensors with an electronic data acquisition process such as CCD/CMOS cameras. Unfortunately, when it concerns imaging systems equipped with a mechanical device (scanning mirrors, magnetic coils, etc.), random scanning methods may be irrelevant owing to acquisition constraints.

To overcome this limitation, the notion of continuous trajectories with variable density samplers is discussed in this section. Continuous and smooth trajectories-based samplers are crucial to extend CS results to a physical implementation, especially for 3D OCT data acquisition and processing. The proposed trajectories are based on spiral, rosette and lissajous scanning schemes which meet certain criteria such as:

- the design scheme should be reconstruction-guidance-based not observation-based;
- the trajectory must be continuous and easily achievable by the scanning system, i.e., considering the kinematics aspects;

- the scanning trajectory must be tunable in terms of sampling rate, length, sampling step, executing time, etc.

In other words, this results in creating proper 2D and 3D subsampling masks (i.e., sensing matrices) **M** for 2D or 3D OCT images, respectively.

2.6. Parametrizable scanning curves

As mentioned above, in this work, we designed three different continuous scanning trajectories (spiral, rosette, and lissajous) (Fig. 3) deemed relevant to ensure an effective CS system while respecting the criteria cited.

There are different ways to implement the chosen scanning continuous curves. Easy tuning of the sampling parameters (sampling rate, step time, length, etc.), can be achieved using the following expressions:

- Spiral:

$$\begin{cases} \boldsymbol{x}(\theta) &= \dfrac{\theta}{d}\cos(\theta) \\ \boldsymbol{y}(\theta) &= \dfrac{\theta}{d}\sin(\theta) \end{cases} \tag{28}$$

with $d \in \mathbb{N}$ allows tuning the distance between two successive spires.

- Rosette:

$$\begin{cases} \boldsymbol{x}(\theta) = k_{max}\ \sin\left(\dfrac{2\pi fz}{z+2}\theta\right)\cos(\theta) \\ \boldsymbol{y}(\theta) = k_{max}\ \cos\left(\dfrac{2\pi fz}{z+2}\theta\right)\sin(\theta) \end{cases} \tag{29}$$

where θ is the curvilinear abscissa, $k_{\max}$ is the curvature, z is the number of rosette's petals.

- Lissajous:

$$\begin{cases} \boldsymbol{x}(\theta) &= a_1\ \sin\left(\dfrac{2\pi f(z-1)}{z}\theta\right) \\ \boldsymbol{y}(\theta) &= a_2\ \sin(2\pi f\theta) \end{cases} \tag{30}$$

where the parameters a_1 and a_2 represent the covered surface size, f determines the base frequency of lissajous curve.

2.7. Rasterization

To be able to successfully apply the designed sensing matrices (i.e., designed masks) and to match the coordinates of the selected measurements to the corresponding ones in the physical OCT device, we implemented a rasterization technique. The latter allows converting continues geometric curves of the vector format of pixels, points, lines, … into an image and *vice-versa*. Among the existing rasterization algorithms, one can cite "Digital Differential Analyzer" (DDA). To meet perfectly the requirements of the proposed methods, we revisited DDA method in order to:

- meet the drawing speed (on-line rasterization) of complex scanning curves;
- convert the drawn trajectory defined in the image (in pixels) to the physical scanning curve (in metric) to be achieved into the sample by the galvanometer mirrors.

Recall that the designed sensing matrices **M** is actually a binary matrix:

$$\mathbf{M}(i,j) = \begin{cases} 1, & \text{acquire an A} - \text{scan at coordinates}(i,j) \\ 0, & \text{do nothing} \end{cases} \tag{31}$$

At the same time, this mask has to be generated from a continuous trajectory. Therefore, it is important to project parametric curve in the discrete basis of mask matrix. Also, the *xy* coordinates of **M** are used in the rasterization algorithm to map the pixels positions (in the image frame) to the metric locations (in the OCT frame) (Fig. 4). Moreover, with the proposed rasterization algorithm it is possible to control the global sampling rate, i.e. the percentage of the measures that will be acquired:

$$p^* = 100 \times \frac{\sum_{i=1}^{h}\sum_{j=1}^{w}\mathbf{M}(i,j)}{\text{Area of the trajectory}} \tag{32}$$

2.8. Coherence evaluation

As discussed in Section 2, the notion of incoherence μ(A) (6) of the observation matrix A of the proposed continuous trajectories sampling (i.e., spiral, rosette, and lissajous) was studied and compared to that of the traditional random sampling matrix. As can be seen in Fig. 5, the numerical values $\mu(A)$ are very close, with a slight difference for the spiral scanning trajectory, this shows that the proposed sensing schemes enjoy sufficiently small coherence and can therefore be considered as relevant for compressed sensing-based recovery.

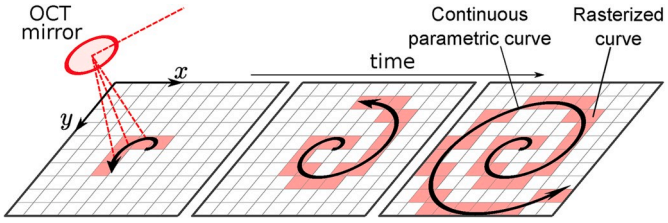

Fig. 4. Illustration of the rasterization algorithm operating in case of a spiral-like scanning trajectory.

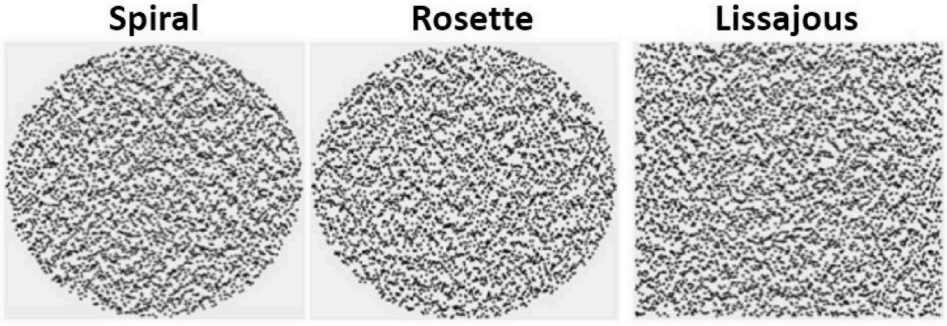

Fig. 3. Illustration of the designed subsampling masks (black dots represent positions of the acquired measurements (20%)).

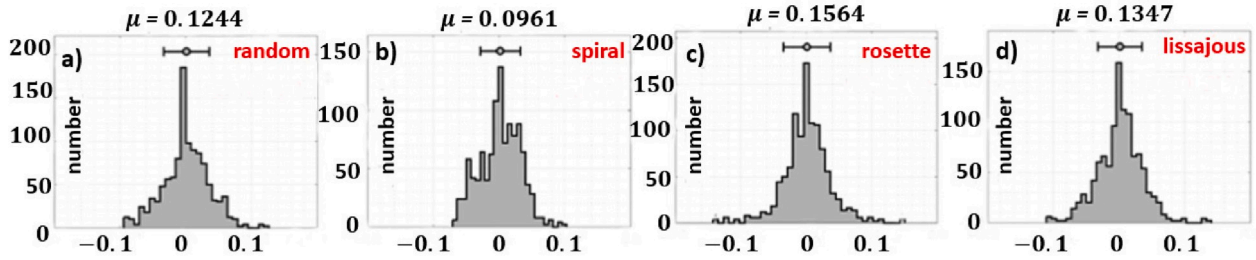

Fig. 5. Comparison of the notion of incoherence between different subsampling methods. The numerical values are obtained for sensing matrices of 105 × 105 pixels.

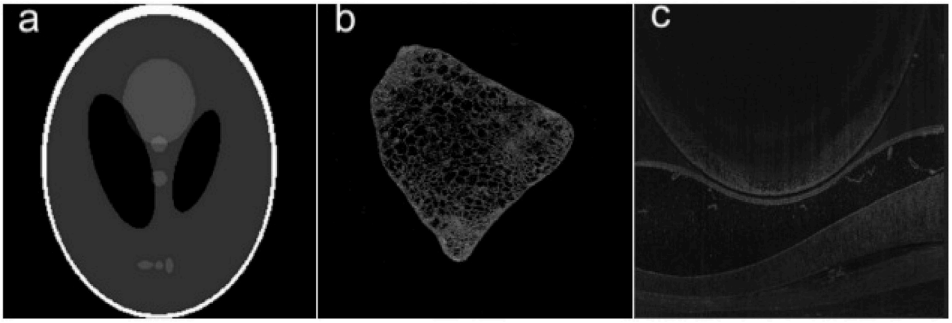

Fig. 6. OCT volumes (here only a 2D slices are depicted) used to access the performances of the proposed algorithm: a) *Shepp-Logan* phantom, b) x — *y* OCT slice of a part of grape, and c) x — *z* OCT slice of the retina of a fish eye.

3. Results and discussion

3.1. Numerical validation using realistic biological data

The proposed methods and materials were firstly validated numerically (in simulation) using ground-truth data. The first validation tests consist of using 2D OCT images of 512 × 512 pixels, while the second uses OCT volumes of 281 × 281 × 199 pixels directly acquired by the Telesto II system.

3.1.1. Evaluation criteria

In order to quantitatively assess the results obtained with different scenarios and OCT images, we implemented two criteria: 1) the peak signal noise ratio (*PSNR*), and 2) the structural similarity index (*SSIM*), which are generally used by the compressed sensing and more widely the image processing communities Miao, Huo and Wilson [31]. The *PSNR* score, given in *db*, is expressed by

$$\mathrm{PSNR} = 10\log_{10}\left(\frac{d^2}{\mathrm{EQM}}\right) \tag{33}$$

where d is the maximal pixel value in the initial OCT image and the *EQM* is obtained by

$$EQM = \frac{1}{hw}\sum_{i=1}^{h}\sum_{j=1}^{w}(\mathbf{I}(i,j) - \mathbf{R}(i,j))^2 \tag{34}$$

with $\mathbf{I}$ representing an initial full-scanned 2D OCT slice (selected from the OCT volume), $\mathbf{R}$ is the reconstructed one.

Furthermore, the *SSIM* score is based on the computation of three values, namely, the brightness l, the contrast c and the structural aspect s. It is given by

$$SSIM = s(\mathbf{R},\mathbf{I})l(\mathbf{R},\mathbf{I})f(\mathbf{R},\mathbf{I}) \tag{35}$$

where,

$$s(\mathbf{R},\mathbf{I}) = \frac{2\sigma_{\mathbf{R}\mathbf{I}} + f_3}{\sigma_{\mathbf{R}}\sigma_{\mathbf{I}} + f_3}, \qquad l(\mathbf{R},\mathbf{I}) = \frac{2\mu_{\mathbf{R}}\mu_{\mathbf{I}} + f_1}{\mu_{\mathbf{R}}^2\mu_{\mathbf{I}}^2 + f_1}, \text{ and } \quad f(\mathbf{R},\mathbf{I}) = \frac{2\sigma_{\mathbf{R}}\sigma_{\mathbf{I}} + f_2}{\sigma_{\mathbf{R}}^2\sigma_{\mathbf{I}}^2 + f_2} \tag{36}$$

with $\mu_{\mathbf{R}}$, $\mu_{\mathbf{I}}$, $\sigma_{\mathbf{R}}$, $\sigma_{\mathbf{I}}$, and $\sigma_{\mathbf{R}\mathbf{I}}$ are the local means, standard deviations, and cross-covariance for images **R, I.** The variables f_1, f_2 and f_3 are small numbers used to stabilize the division with weak denominator.

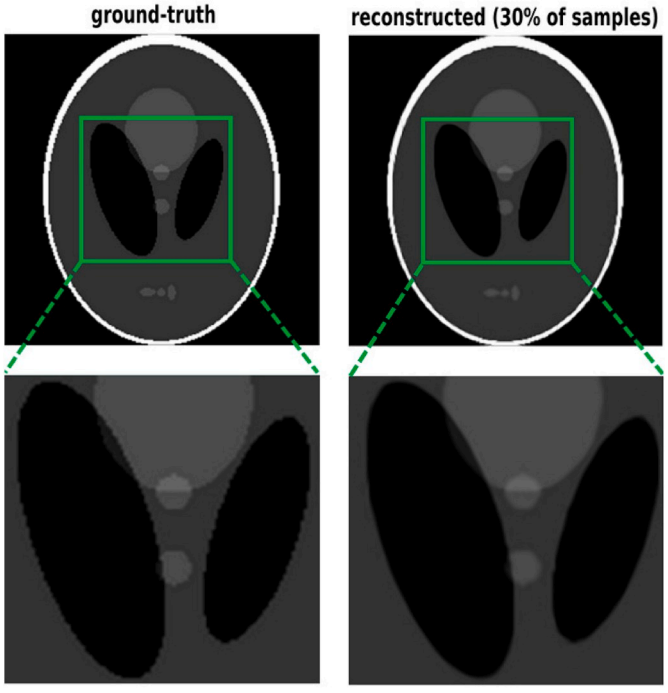

Fig. 7. [Sheep-Logan phantom] Comparison between (a) the original image and (b) the reconstructed one using 30% of measurements.

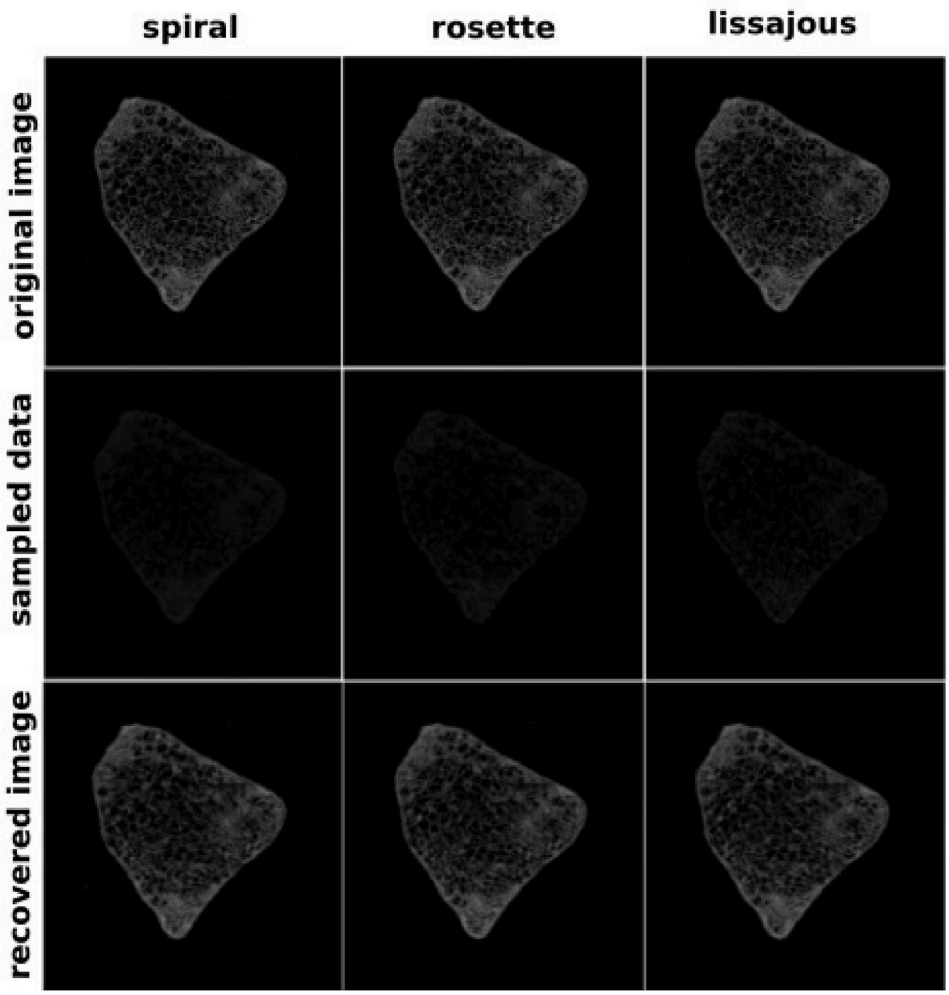

Fig. 8. [Grape] Reconstruction of OCT image using 20% of measurement and different subsampling techniques.

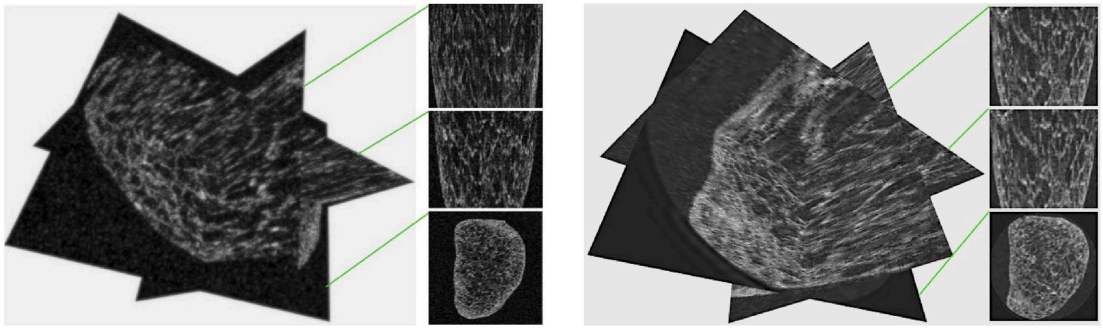

(a) Original OCT volume (b) Reconstructed OCT volume

Fig. 9. Visual comparison between the original and the reconstructed OCT volumes.

3.1.2. Numerical validation: 2D images

The numerical validation was performed following several scenarios. First of all, as inputs in the proposed algorithm we used three OCT volumes (only 2D slice images are depicted for a better visualization) shown in Fig. 6. Note that the first image (Fig. 6(a)) is the "*Shepp-Logan*" phantom, which is generally used in the literature dealing with medical image processing and CS. In addition, two OCT images of biological samples (i.e., part of grape and retina of a fish eye) were also used in this validation.

First, for each image test, we applied the proposed CS method using various subsampling rate ranging from 10% to 70% with a step of 10% defined using the constructed masks based the developed continuous trajectories introduced in Section 2.4. The obtained results are presented and discussed in the following.

3.1.2.1. Shepp-Logan phantom (30% of measurements). The first numerical validation consisted of the reconstruction of the Shepp-Logan phantom image using 30% of measurements. The latter were obtained using the continuous subsampling trajectories. In Fig. 7, are compared the original (ground-truth) image (Fig. 7(a)) and the reconstructed one

Table 1
Quality evaluation of the validation tests on both the retina of a fish eye and the Shepp-Logan phantom images using different subsampling rates and scanning trajectories.

subsampling rate (%)	continuous trajectory type	image type			
		retina of a fish eye		Shepp-Logan phantom image	
		PSNR (db)	*SSIM*	*PSNR* (db)	*SSIM*
10%	rosette	38.944	0.834	40.771	0.973
	spiral	39.059	0.833	41.440	0.974
	lissajous	37.825	0.859	40.908	0.973
20%	rosette	39.902	0.849	41.730	0.976
	spiral	39.961	0.847	42.171	0.978
	lissajous	38.911	0.882	41.790	0.977
30%	rosette	41.048	0.868	42.472	0.980
	spiral	41.129	0.870	42.827	0.982
	lissajous	40.103	0.910	42.420	0.981
50%	rosette	43.361	0.898	44.043	0.987
	spiral	43.767	0.903	44.891	0.989
	lissajous	42.006	0.945	44.004	0.988
70%	rosette	45.921	0.917	45.278	0.991
	spiral	45.893	0.917	45.436	0.991
	lissajous	44.202	0.969	45.073	0.991

(Fig. 7(b)). As can be noticed, the recovered image (using the spiral subsampling method) is faithful to the ground-truth one. This is confirmed by the zoom-in thumbnail image. The second remark is that in the reconstructed image, the edges appear smoother than to those of the original image. Finally, the obtained results are very similar using the other two subsampling methods.

The qualitative study of the obtained results are discussed in Section 3.2 using the similarity scores, i.e., the *PNSR* and the *SSIM*.

3.1.2.2. Grape (20% of measurements). Similarly, the CS method was validated using OCT images of a part of a grape. In this test, the subsampling rate is of 20%. The reconstructed images are depicted in Fig. 8: from left to right, using the spiral, the rosette, and the lissajous trajectories subsampling methods, respectively. Again, one can highlighted the recovered OCT images are very similar to ground-truth ones. Note that, even the recovered images still similar from one subsampling method to another, lissajous-based sensing matrix appears more interesting because it covers the entire OCT field-of-vision compared to both the spiral and rosette methods.

3.1.3. Numerical validation: volumes

The proposed methods were also validated using directly the OCT volume instead of individual 2D slices (B-Scans) as input of the proposed algorithm. One can compare the reconstructed OCT volume with the ground-trust one as can be seen in Fig. 9. It can be concluded that the recovered volume (using 30% of measurements) is very similar to the original one.

3.2. Quantitative analysis

To assess the performances of the proposed compressed sensing algorithm, we conducted numerous validation tests using both the different types of masks (i.e., spiral, rosette, and lissajous) and various subsampling rates: 10%, 20%, 30%, 50%, and 70%. For each test, we computed the values of both the *PSNR* and *SSIM* (introduced at the beginning of this Section). Then, Table 1 summarizes the obtained numerical values of each test using both the retina of a fish eye and "Shepp-Logan" phantom images as inputs on the CS algorithm. Note that, generally, if the *PSNR* values are typical between 30 db and 50 dB (for 8-bits encoded images), then reconstructed image is considered faithful to the original one. Also, when the *PSNR* is equal or greater to 40 db, as

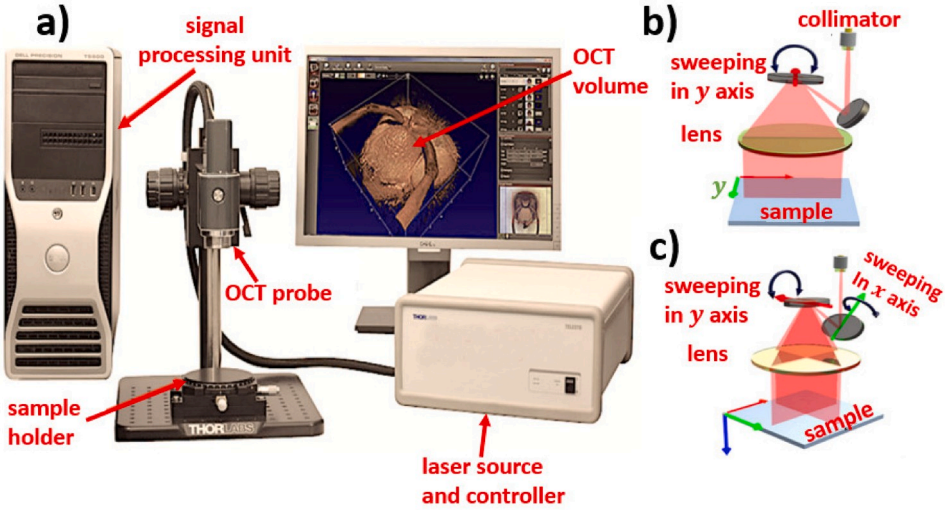

Fig. 10. a) the global view of the OCT device (b–c) depicts the both the B-scan and C-scan acquisition modes, respectively.

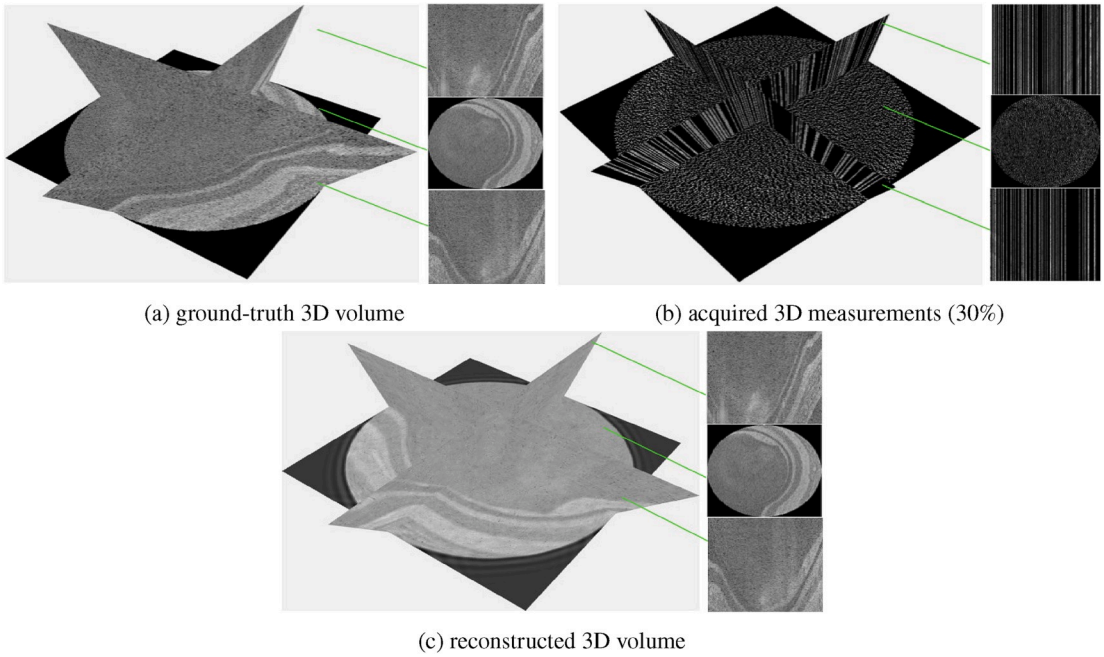

(a) ground-truth 3D volume (b) acquired 3D measurements (30%)

(c) reconstructed 3D volume

Fig. 11. Experimental validation using a fish eye as biological sample (30% of measurements).

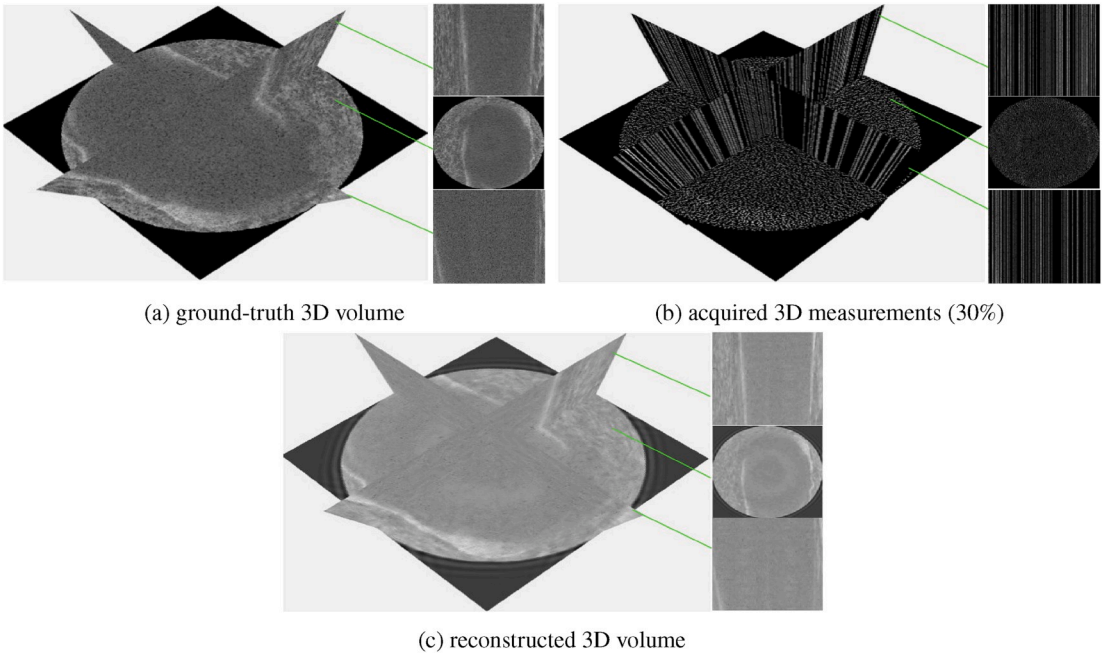

(a) ground-truth 3D volume (b) acquired 3D measurements (30%)

(c) reconstructed 3D volume

Fig. 12. Experimental validation using a part of grape as biological sample (30% of measurements).

consequence the quality of the reconstruction is qualified as similar to the original image.

As can be underlined the obtained *PSNR* values vary from approximately 40 db for 10% of data to 45 db for 70% of data. The first remark is that even for only 10% of samples, the quality of the reconstructed image/volume is very interesting. This is confirmed by the second similarity score (i.e., *SSIM*) with numerical values varying from 0.97 to 0.99 for 10%–70% of samples, respectively. The *SSIM* values are also interesting even only 10% of measurements are used during the recovery task. Remember that, generally, *SSIM* numerical values are in the range of [–1, 1], where value 1 (respectively, −1) is reachable when the similarity, between the compared images, is "perfect".

Furthermore, the rosette and spiral sampling patterns only acquire $\frac{\pi}{4}$ region of k-space due to their circular *k*-space support, as compared to lissajous method. This factor is considered in the computation of the subsampling rate for each trajectory. The same performances assessment was achieved using the OCT image acquired on the fish eye. The *PSNR* and *SSIM* numerical values are reported in Table 1 in which one can highlighted that the results are very similar to those obtained for the "Sheep-Logan" phantom image. Again, the spiral-scanning trajectory gives better results comparing to rosette and lissajous.

4. Experimental validation

4.1. Experimental setup

The proposed materials and methods were validated in both simulation and experimentally. To carry out the experimental implementation of the CS algorithm, we designed a robotic setup which acts as a positioning platform combined with an OCT device, the Telesto II from Thorlabs® (Fig. 10(a)). The latter consists of a **FD-OCT** system which offer three types of acquisition modes: A-scan (1D optical core), B-scan (2D cross-sectional image) and C-scan ($(n \times m \times k)$ volume). In fact, the Telesto II system is based on the principle of low-coherence interferometry because the velocity of light is extremely high. The low-coherence i.e., high-bandwidth light beam is directed to the target tissue and the scattered back-reflected light is combined with a second beam (reference beam), which was split off from the original light beam. The resulting interference patterns are used to reconstruct the A-scan. The latter represents the axial resolution in the tissue, of about 1–15 μm Drexler and Fujimoto [32]. In addition, the light beam is able to move along the tissue in *xy* directions. This results in a compilation of A-scans with each of them having a different incidence point. From these series of A-scans, a two-dimensional cross-sectional image of the target tissue can be reconstructed which known as a B-scan. Moreover, a C-scan acquisition consists of the concatenation of parallel B-scans as summarized in Fig. 10(b and c).

4.2. Validation using a physical system

The experimental validation scenario is performed as follows: instead of using prerecorded images or volumes with further off-line subsampling them (using sensing matrices) to create the sparse data, we directly (on-line) controlled the galvanometer mirrors of the OCT probe to acquire sequentially only a limited number of measurements (A-Scans) following a predefined continuous trajectory. The *xy* coordinates (pixels at 1 in the sensing matrix) of rasterized trajectory are used as the inputs control of the galvanometer mirrors. As claimed previously, it is possible to tune the scanning trajectories parameters in aim to manage the acquisition rate (expressed as a percentage of the entire volume).

The first experiment was conducted by acquiring 30% of samples on the fish eye. The latter was placed under the OCT probe. Therefore, instead of acquiring the entire data, we controlled the galvanometer mirrors of the OCT device to acquire only 30% of measurements under a continuous trajectory (here a spiral). To do this, we used a spiral-scanning trajectory. Actually, each position $p = (x, y)$ of the rasterized trajectory is considered as the control input of the galvanometer mirrors. In Fig. 11 is depicted simultaneously, the ground-truth OCT volume (acquiring using 100% of data), the 30% acquired data, and the reconstructed OCT volume. One can remark that the reconstructed volume is faithful to the ground-truth one.

In the second experimental test, we changed the retina sample by a part of a grape (less translucent sample compared to the retina). The obtained results are shown in Fig. 12. Again, the reconstructed OCT volume (Fig. 12(c)) is of good accuracy compared to the ground-truth one (Fig. 12(a)).

4.3. Discussion

The obtained results are satisfactory according to the metric evaluation criteria. It has been shown that it is possible to design non-random sampling matrices that are compatible with the physical implementation as widely studied in the related literature Donoho [7]; Candes et al. [36]; Rauhut [29]. The studied sensing matrix offer similar features in terms of sparsity and incoherence comparing to the well-established random or pseudo-random methods.

In addition, bi-dimensional shearlet Duflot et al. [25] and wavelet Chitchian, Fiddy and Fried [33] decomposition were studied the sparsity tool in CS paradigms applied to improve 2D OCT acquisition. However, to the best of our knowledge, it was the first time that tri-dimensional shearlet decomposition was implemented in a physical OCT system. Additionally, continuous trajectories combined with rasterization technique were already reported in the literature, however, they were designed to operate off-line using recorded image data Chauffert, Ciuciu, Kahn and Weiss [34].

Furthermore, the developed CS algorithm is not specific to optical coherence tomography modality but can also be used in different 3D imaging methods such as MRI or CT-scan. As a consequence, we evaluated the CS algorithm with 3D sensing matrices more compatible with the acquisition scheme of this type of imaging devices (i.e., MRI and CT).

Although the proposed methods and materials are intended to improve the acquisition frame-rate of an OCT imaging system, there are still improvements/optimizations to be considered. For instance, some parts of the CS algorithm consume much computation time, in particular those relating to the Fourier transform and its inverse. These parts can be implemented directly on a GPU Blanchard and Tanner [35] to save up to 10 times more computing time.

5. Conclusion

In this paper, in order to overcome the limitations of an **FD-OCT** acquisition system, we proposed a new compressed sensing paradigm. The developed methodology consisted of four main parts: 1) design of different continuous scanning trajectories (off-line), 2) rasterize the subsampling trajectories to meet the physical conditions (off-line), 3) transform the OCT measurements in the shearlet supports for sparsifying, and 4) recover the entire OCT data using only few *k-sparse* data (on-line).

The proposed Compressed Sensing algorithm was successfully validated numerically and experimentally. First, this algorithm was evaluated: 1) quantitatively using various subsampling rate (from 10% to 70%) obtained thanks to the designed continuous scanning trajectories (e.g., spiral, rosette, and lissajous), and 2) qualitatively using similarity scores such as *PSNR* and *SSIM* computed for each scenario (OCT image, subsampling rate, scanning trajectory type, etc.).

As claimed, the CS algorithm was also implemented directly on a commercial FD-OCT system. This means that, the galvanometer mirrors that equip the OCT system were controlled directly (using the *xy* coordinates of the scanning trajectories as inputs on the control loop) to acquire a limited number of A-scans. This data was then used to recover the whole OCT volume.

The obtained results in both simulation and experiments showed promising performance in terms of quality of the reconstructed OCT images and volumes. This fact is also confirmed by comparing the obtained reconstruction with the ground-truth data.

Future work will consist of the optimization of the CS code to improve its execution time. Actually, several parts of the algorithms were scripted without optimization in a **MatLab** framework. The ideal would be to implement the current scripts in C++ or in GPU (Graphic Processing Unit) for the direct and inverse shearlet transform.

Declaration of competing interest

The authors declare that they have no conflicts of interest.

Acknowledgment

This work was supported by the French “Agence Nationale de la Recherche (ANR)” through the NEMRO project [ANR-14-CE17-0013-001] and the INSERM ROBOT Project: ITMO Cancer no 17CP068-00.

References

[1] Fujimoto JG, Pitris C, Boppart SA, Brezinski ME. Optical coherence tomography: an emerging technology for biomedical imaging and optical biopsy. Neoplasia 2000;2:9. https://doi.org/10.1038/sj.neo.7900071.

[2] Zysk AM, Nguyen FT, Oldenburg AL, Marks DL, Boppart SA. Optical coherence tomography: a review of clinical development from bench to bedside. J Biomed Optic 2007;12:051403. https://doi.org/10.1117/1.2793736.

[3] Wang C, Xia X, Tian B, Zhou S. Comparison of fourier-domain and time-domain optical coherence tomography in the measurement of thinnest corneal thickness in keratoconus. Journal of ophthalmology 2015. https://doi.org/10.1155/2015/402925. 2015.

[4] Chen TC, Cense B, Pierce MC, Nassif N, Park BH, Yun SH, White BR, Bouma BE, Tearney GJ, de Boer JF. Spectral domain optical coherence tomography: ultra-high speed, ultra-high resolution ophthalmic imaging. Arch Ophthalmol 2005;123:1715–20. https://doi.org/10.1001/archopht.123.12.1715.

[5] Choma MA, Sarunic MV, Yang C, Izatt JA. Sensitivity advantage of swept source and fourier domain optical coherence tomography. Optic Express 2003;11:2183–9. https://doi.org/10.1364/oe.11.002183.

[6] Liu X, Kang JU. Compressive sd-oct: the application of compressed sensing in spectral domain optical coherence tomography. Optic Express 2010;18:22010–9. https://doi.org/10.1364/oe.18.022010.

[7] Donoho DL. Compressed sensing. IEEE Trans Inf Theor 2006;52:1289–306. https://doi.org/10.1109/tit.2006.871582.

[8] Candes EJ, Romberg JK, Tao T. Stable signal recovery from incomplete and inaccurate measurements. Commun Pure Appl Math: A Journal Issued by the Courant Institute of Mathematical Sciences 2006;59:1207–23. https://doi.org/10.1002/cpa.20124.

[9] Foucart S, Rauhut H. A mathematical introduction to compressive sensing. Birkhauser Basel 2013;1. https://doi.org/10.1007/978-0-8176-4948-7.

[10] Davenport M, Duarte M. In: eldar y, andg kutyniok, editors. Introduction to compressed sensing; 2012. https://doi.org/10.1017/cbo9780511794308.002 [chapter 1] of compressed sensing: Theory and applications.

[11] Fei Y, Wei G, Zongxi S. Medical image fusion based on feature extraction and sparse representation. Int J Biomed Imag 2017. https://doi.org/10.1155/2017/3020461. 2017.

[12] Mallat SG. A theory for multiresolution signal decomposition: the wavelet representation. IEEE Trans Pattern Anal Mach Intell 1989;11:674–93. https://doi.org/10.1109/34.192463.

[13] Labate D, Lim WQ, Kutyniok G, Weiss G. Sparse multidimensional representation using shearlets. In: Wavelets XI. International Society for Optics and Photonics; 2005. 59140U. https://doi.org/10.1117/12.613494.

[14] Kutyniok G, Labate D. Introduction to shearlets. In: Shearlets. Springer; 2012. p. 1–38. https://doi.org/10.1007/978-0-8176-8316-0_1.

[15] Candes EJ. The restricted isometry property and its implications for compressed sensing. Compt Rendus Math 2008;346:589–92. https://doi.org/10.1016/j.crma.2008.03.014.

[16] Bigot J, Boyer C, Weiss P. An analysis of block sampling strategies in compressed sensing. IEEE Trans Inf Theor 2016;62:2125–39. https://doi.org/10.1109/tit.2016.2524628.

[17] Kutyniok G, Lim WQ, Reisenhofer R. Shearlab 3d: faithful digital shearlet transforms based on compactly supported shearlets. 2014. https://doi.org/10.1145/2740960. arXiv preprint arXiv:1402.5670.

[18] Cohen A, Dahmen W, DeVore R. Compressed sensing and best fc-term approximation. J Am Math Soc 2009;22:211–31. https://doi.org/10.1090/s0894-0347-08-00610-3.

[19] Juditsky A, Nemirovski A. On verifiable sufficient conditions for sparse signal recovery via ϵ 1 minimization. Math Program 2011;127:57–88. https://doi.org/10.1007/s10107-010-0417-z.

[20] d'Aspremont A, El Ghaoui L. Testing the nullspace property using semidefinite programming. Math Program 2011;127:123–44. https://doi.org/10.1007/s10107-010-0416-0.

[21] Candès EJ, Plan Y, et al. Near-ideal model selection by ϵ_1 minimization. Ann Stat 2009;37:2145–77. https://doi.org/10.1214/08-aos653.

[22] Chrétien S, Darses S. Sparse recovery with unknown variance: a lasso-type approach. IEEE Trans Inf Theor 2014;60:3970–88. https://doi.org/10.1109/tit.2014.2301162.

[23] Blumensath T, Davies ME. Iterative hard thresholding for compressed sensing. Appl Comput Harmon Anal 2009;27:265–74. https://doi.org/10.1016/j.acha.2009.04.002.

[24] Maleki A. Coherence analysis of iterative thresholding algorithms. In: 2009 47th annual allerton conference on communication, control, and computing (allerton). IEEE; 2009. p. 236–43. https://doi.org/10.1109/allerton.2009.5394802.

[25] Duflot LA, Krupa A, Tamadazte B, Andreff N. Shearlet transform: a good candidate for compressed sensing in optical coherence tomography. In: Engineering in medicine and biology society (EMBC), 2016 IEEE 38th annual international conference of the. IEEE; 2016. p. 435–8. https://doi.org/10.1109/embc.2016.7590733.

[26] Candes EJ, Donoho DL. Curvelets: a surprisingly effective nonadaptive representation for objects with edges. Technical Report. Stanford Univ Ca Dept of Statistics; 2000. https://doi.org/10.1155/2017/3020461.

[27] Kittipoom P, Kutyniok G, Lim WQ. Construction of compactly supported shearlet frames. Constr Approx 2012;35:21–72. https://doi.org/10.1007/s00365-011-9142-y.

[28] S H, G S. Fast finite shearlet transform: a tutorial. Arxiv Math; 2014. p. 1–41.

[29] Rauhut H. Compressive sensing and structured random matrices. Theoretical foundations and numerical methods for sparse recovery 2010;9:1–92. https://doi.org/10.1515/9783110226157.1.

[30] Candes EJ, Plan Y. A probabilistic and ripless theory of compressed sensing. IEEE Trans Inf Theor 2011;57:7235–54. https://doi.org/10.1109/tit.2011.2161794.

[31] Miao J, Huo D, Wilson DL. Quantitative image quality evaluation of mr images using perceptual difference models. Med Phys 2008;35:2541–53. https://doi.org/10.1118/1.2903207.

[32] Drexler W, Fujimoto JG. State-of-the-art retinal optical coherence tomography. Prog Retin Eye Res 2008;27:45–88.

[33] Chitchian S, Fiddy M, Fried NM. Wavelet denoising during optical coherence tomography of the prostate nerves using the complex wavelet transform. In: 2008 30th annual international conference of the IEEE engineering in medicine and biology society; 2008. p. 3016–9. https://doi.org/10.1109/IEMBS.2008.4649838.

[34] Chauffert N, Ciuciu P, Kahn J, Weiss P. Variable density sampling with continuous trajectories. SIAM J Imag Sci 2014;7:1962–92. https://doi.org/10.1137/130946642.

[35] Blanchard JD, Tanner J. Gpu accelerated greedy algorithms for compressed sensing. Mathematical Programming Computation 2013;5:267–304. https://doi.org/10.1007/s12532-013-0056-5.

[36] Candes EJ, Romberg J, Tao T. Robust uncertainty principles: exact signal reconstruction from highly incomplete frequency information. IEEE Trans Inf Theor 2006;52:489–509. https://doi.org/10.1109/tit.2005.862083.